Star tracker accuracy improvement and optimization for attitude measurement in three-axis

Michael J. Lichter
Air Force Institute of Technology, Dayton OH
NASA Glenn Research Center, Cleveland OH

ABSTRACT

High precision attitude measurement systems obviate the need for a beacon from the receiver making it possible for the spacecraft to beam a laser communications signal to a ground station without the ground station advertising its location. The research presented targets new detection and estimation methods to improve the accuracy in locating stars on a focal plane detector (FPD), and an understanding of the effects of changes in the optics design parameters and aberration, including defocus, on the navigation solution itself. This understanding can lead to an optimization of the attitude solution with respect to those optics realm parameter changes. The methodology discussed includes the development of a model of a current star tracker system. Using this model, multiple algorithms are implemented, including a multi-hypothesis method (MHT), to detect and estimate the position of the stars on the FPD. It will be shown that using the MHT for detection and estimation, a greater accuracy can be found for each star estimation from more traditional detection and estimation algorithms. The approach then uses the model to develop statistics of the star tracker and the attitude estimation outputs to understand the accuracy, or variance, of the system's attitude solution. This solution is repeated for a range of defocus aberration, and a lower limit to the variance of the attitude solution is shown. A Cramer Rao lower bound solution is derived for the star tracker system and the results are compared to the Monte Carlo analysis from the model and shown to correlate very well. The approach uses a star image not as a Gaussian spot on the focal plane as done in previous work, and use of an image that includes the effects of aberrations of the optic system, and the effects of under-sampling and noise from the FPD as well. Analysis includes exploring a star tracker's accuracy improvement through the combination of focus error and under-sampling effects, possibly contradicting conventional wisdom and approaches.

1. INTRODUCTION

Missions into space generate an ever increasing amount of information. These missions continue to develop more sophisticated scientific instrumentation which usually means they generate more data, through high definition images, spectrometers, etc. The imaging and remote sensing capabilities have far outpaced the ability to transmit the resulting data back to Earth, and this is especially true in deep space. To accommodate this need, NASA has been migrating to higher bandwidth radio frequencies (RF) spectrum utilization, along with increasing the size of its antennas and power of it radio transmitters, pushing the limits of what they can achieve. Even with the higher bandwidths, missions are leaving data in space and unable to deliver it to Earth where it can be used. As an example, a high resolution image taken by the Mars Reconnaissance Orbiter (MRO) transmitted at its maximum data rate of 6 Mbit/s takes nearly 1.5 hours to transfer to Earth. In contrast, a 100 Mbit/s optical communications solution could transfer that same image in less than 5 minutes.

Current laser communication systems require an active beacon from the receiver so that the transmitter can find and point at the receiver and maintain the link. This technique does not translate well to missions which are in deep space. The further the distance into space, the higher the power needed for a beacon from the ground. At some point the distance causes a beacon system to become impractical and unwieldy; this due to the power needed, and the coordination and safety aspects of the overall system operation. This aspect of the system design is pushing optical communications to beaconless systems.

There are challenges that come with using an optical beam. The shorter wavelength means a narrower beam, so pointing of that beam becomes more of a challenge compared to RF. A demonstration of a laser communication

system was achieved by the Lunar Laser Communication Demonstration [1] [2], which operated in Lunar orbit in 2013-14. It successfully communicated with an Earth ground station in New Mexico using a laser. The laser covered a 6 km diameter area inside the state of NM, compared to an RF signal which would cover the entire Western United States. Therefore the precise pointing of the beam is the paramount challenge of optical communications.

The combination of the need for a beaconless system and the smaller divergent optical beam has created a need to know, with great accuracy, both the orientation of the spacecraft and the laser beam pointing direction. A system has been proposed to do this and is called the Integrated Radio and Optical Communications (iROC) system [3] [4]. An illustration of a beaconless deep space satellite is shown in Figure 1. This system uses a star tracker to measure very accurately the attitude of the spacecraft and uses that information to precisely point the laser beam back to Earth to the ground station, without the use of a beacon. However, the attitude measurement system required for this type of system must be capable of realizing very accurate attitudes, on the order of a few μrads [4]. Note in the figure, a comparison is made of an optical beam with that of an example RF beam that might be used for the same system [5]. This illustrates the challenge of locating and pointing the transmission beam for the much smaller diameter optical beam compared to that of the RF beam.

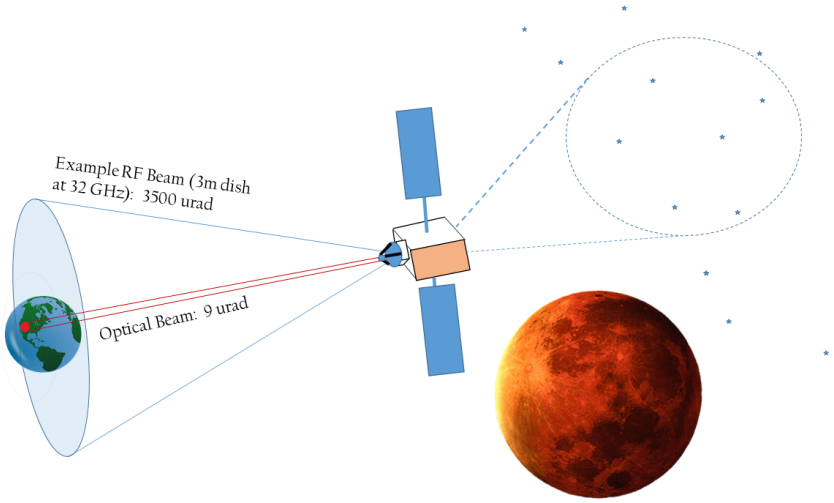


Fig. 1: Deep Space Beaconless Laser Communications Example, with comparison of RF and optical beams [5]

Improvements to spacecraft attitude estimation using star trackers might make this possible. High precision attitude measurement systems obviate the need for the beacon from the receiver making it possible for the spacecraft to beam a laser signal to a ground station without the ground station sending a high power beacon signal to deep space.

Most spacecraft today rely on star tracker sensors for three axis absolute measurement for their closed loop control systems for pointing control. These sensors are considered to be the most accurate sensors available [6].

2. STAR TRACKER MODEL

The typical star tracker system illustration under consideration is shown in Figure 2.

2.1 Star Source

To model the star source, the measure of apparent magnitude will be used and compared to that of a known star. This measure uses the apparent brightness which is the flux of the star within a spectral band as seen by a sensor on earth. This is represented by the number of photons received at the receiver. Given that the star has an intrinsic luminosity at its source, L, measured in Joules per second (or Watts), and the star is some distance away, d_s, the apparent brightness, B_r, follows the inverse square law of light

The apparent magnitude scale was originally defined by Hipparchus over 2100 years ago when he defined relatively bright stars to have a magnitude of 1, and the faintest stars to be of magnitude of 6. Note the inverse relationship

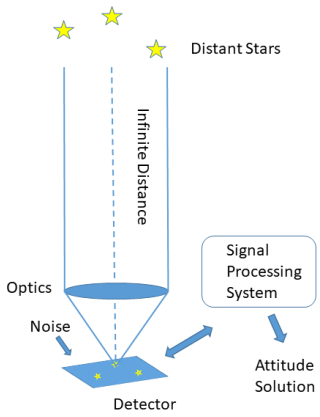


Fig. 2: The Star Tracker System illustration with Inputs and Outputs.

between the scale and the brightness. This same scale has remained to this day and through measurements it is found that the apparent brightness between a magnitude 1 and a magnitude 6 star has a factor of 100 difference. This results in a single unit of the apparent magnitude being the fifth root of 100, $\sqrt[5]{100} \approx 2.512$ (an irrational number). It is desirable to compare the brightness from a known star with magnitude zero, to an unknown star to determine its magnitude, due to the simplification in the math it creates. The blackbody modeling of Vega will be used as a reference, which is essentially a zero magnitude star [7]. The process of determining the apparent magnitude of the star is to measure the photons received from it and the photons received from Vega and inserting it into the following equation

$$m_x = -2.5 \log_{10} \frac{B_x}{B_{xo}} \tag{1}$$

where B_x is the number of photons (apparent brightness) received from the star we are measuring, and has a specific spectral bandwidth x, B_{xo} is the number of photons received from a known star with magnitude of 0, in this case Vega, again with the same spectral bandwidth, m_x is the apparent magnitude of the measured star.

2.2 Optical Propagation

The optical propagation of a light wave generated from a star that arrives at the star tracker sensor, through its optics, will now be discussed.

Figure 3 shows the coordinate system convention used in the following analysis of an imaging system.

The imaging geometry discussed will be aided by Figure 4 to show the notation to be used.

To determine an impulse response for an optical system, one can model a point source at (ξ, η) by a spherical wave emanating from that point with a paraxial approximation of that wave written as [8, p. 110]

$$U_l(x,y) = \frac{1}{j\lambda z_1} exp\left[-j\frac{\pi}{\lambda z_1}((x-\xi)^2 + (y-\eta)^2) \right] \tag{2}$$

A spherical lens can be modeled using the lens transformation defined in [8, p. 101], which approximates the spherical surfaces of the lens by parabolic surfaces; this is represented by the phase transformation

$$U_{LT}(x,y) = exp[-j\frac{\pi}{2\lambda f}(x^2 + y^2)], \tag{3}$$

where f is the focal length of the lens.

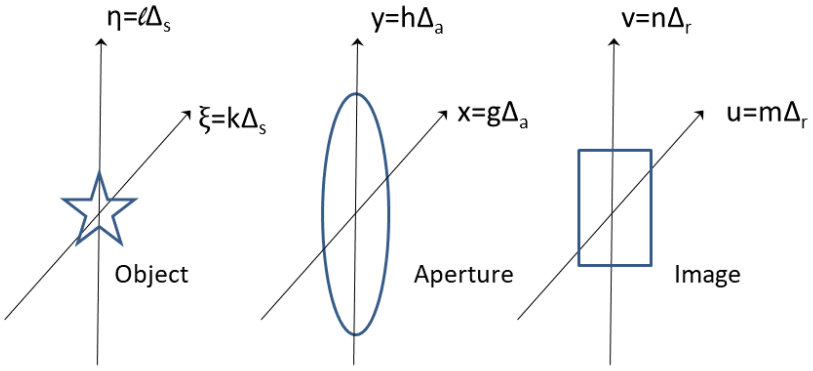


Fig. 3: Imaging System Coordinates used in Imaging Analysis.

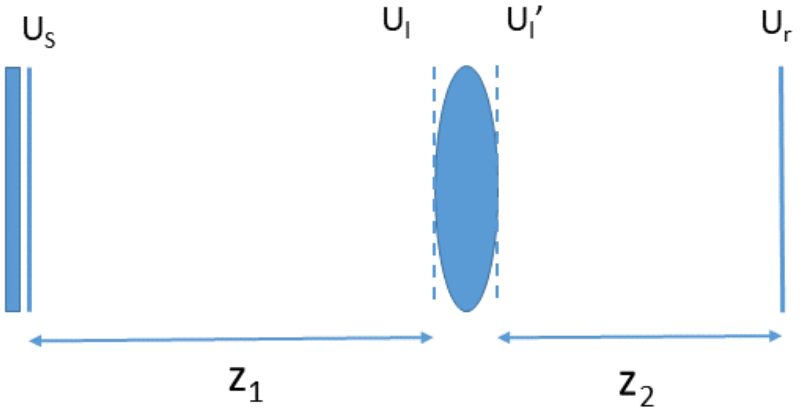


Fig. 4: Notation for Geometry of Image Formation.

Therefore, using this transformation, the wave coming out of the lens at U_l' (from Figure 4) is given by

$$U_l'(x,y) = U_l U_{LT} \tag{4}$$

Using this wave out of the lens and inserting that into a Fresnel diffraction equation for the propagation over the distance of z_2, an analytical solution is found. However, it is found that if the lens law is satisfied by the optical system (the system is focused), and certain conditions are met as outlined in [8, pp. 111-113], the impulse response is simplified to be a Fraunhofer diffraction pattern of the lens aperture, centered on image coordinates (u,v) as shown here [8, p. 113]

$$h_a(u,v;\xi,\eta) = \frac{1}{\lambda^2 z_1 z_2} \iint_{-\infty}^{+\infty} P(x,y) exp\Big[-j\frac{2\pi}{\lambda z_2}[(u-M\xi)x + (v-M\eta)y]\Big] dxdy \tag{5}$$

where there is an additional scaling factor of $1/\lambda^2 z_1 z_2$.

Note that the star location on the image plane, u_1, v_1 is represented by the geometrical optics relationship of $M\xi, M\eta$, respectively, where M is the transverse magnification of the system.

To model an imperfect circular lens to represent the phase distortions of light passing through it, a set of orthonormal Zernike polynomials will be used. Each polynomial represents a type of phase distortion, and these distortions can be added up, each weighted by a coefficient to give the total phase distortion of the lens, θ_o, as follows [9]

$$\theta_o(g,h) = \sum_j a_j Z_j(g,h) \tag{6}$$

where the a_j is the weighting coefficient of the j^{th} Zernike polynomial $Z_j(g,h)$. To model the distortions of the lens, one would add the phase found in Equation (6) to the U_{LT} term in Equation (3) to represent the field just after the lens transformation. Therefore, as an example, and to be used in later sections, if one wanted to add a focus aberration, which is the $j = 4$ term, the following term would be multiplied to Equation (4) as follows

$$U_a(x,y) = U_l' exp\Big(j\frac{2\pi}{\lambda}\theta_{o4}(x,y)\Big) \tag{7}$$

where U_a is the aberrated wavefront coming out of the lens, θ_{o4} is Equation (6) evaluated at $j = 4$.

Goodman [8, p. 133] addresses the linearity of optical systems for when the illumination is coherent and incoherent. A coherent imaging system is linear in complex amplitude and its impulse response is called the amplitude impulse response. An incoherent imaging system is linear in intensity and its impulse response of such a system is the squared magnitude of the amplitude impulse response, and is called the Optical Transfer Function (OTF). This can be understood heuristically by considering that illumination that is spatially coherent has various impulse responses in the image plane that are varying in unison, and thus they must be added on a complex amplitude basis; making this situation linear in complex amplitude. For the spatially incoherent case, the various impulse responses in the image plane vary in uncorrelated ways, and thus they must be added on an intensity basis.

Since the star creates an optical wave that is spatially incoherent, from [8, p. 135], and the previous discussion, the imaging system is linear in intensity. Because of this, the convolution can be used as follows

$$I_r(u,v) = \iint_{-\infty}^{+\infty} I_s(\xi,\eta)|h_a(u-\xi, v-\eta)|^2 d\xi d\eta \tag{8}$$

which is a convolution of input intensity with the intensity impulse response, where $h_a(u-\xi, v-\eta)$ is the amplitude impulse response of the system, I_s is the input or source intensity signal, and I_r is the output or received intensity signal. The intensity or power value is what is received at the focal plane detector (FPD) in practice. The intensity impulse response is found by the squared modulus of the amplitude impulse response.

The discrete form of the calculated power at the detector with a properly sampled or Nyquist sampled detector, referencing the continuous form of Equation (8), is shown in the following convolution of the input power waveform with the point spread funcntion (PSF) waveform to get the resulting power waveform with the diffraction effects

$$I_r(m_1,n_1) = \Delta_s^2 \sum_{m=1}^{N}\sum_{n=1}^{N} I_s(m,n) h(m_1\Delta_r - m\Delta_s, n_1\Delta_r - n\Delta_s) \tag{9}$$

where h is the intensity PSF of the system, and the I_s is the Intensity of the source. The values of m and n are the coordinate indices of the input source points and m_1 and n_1 are detector plane pixel indices, and as mentioned earlier they are multiplied by the usually implied Δ_r (assumed that the u and v directions are sampled spatially with the same size) to create the actual coordinate.

In the frequency domain, Equation (8) this simplifies to:

$$\mathscr{F}\{I_r\} = \mathscr{F}\{I_s\}\mathscr{F}\{|h_a(u,v)|^2\} = \mathscr{F}\{I_s\}\mathscr{H}(f_u, f_v) \tag{10}$$

where the $\mathscr{F}\{|h_a(u,v)|^2\}$ is the OTF, $\mathscr{H}(f_u, f_v)$.

One can now find the intensity PSF by taking the magnitude squared of the field (or amplitude) PSF and normalize it. Looking at Equation (10), the $\mathscr{H}(f_u, f_v)$, using this PSF is found as follows:

$$\mathscr{H}(f_u, f_v) = \frac{\mathscr{F}\{|h_a(u,v)|^2\}}{\iint_{-\infty}^{+\infty} |h_a(u,v)|^2} \tag{11}$$

Therefore, to complete the goal of finding the overall $h_a(x,y)$ to use in determining the OTF of the system for frequency analysis, one can use the unaberrated amplitude PSF from Equation (5), and apply the aberration using Equation (7). The use of the Riemann sum representation of Equation (5) will be used to prepare for its use in computational analysis. The result is found to be

$$h_a(m-a, n-a) = \frac{\Delta_a^2}{\lambda^2 z_1 z_2} \sum_{g=1}^{N} \sum_{h=1}^{N} P(g\Delta_a, h\Delta_a) exp\Big(j\frac{2\pi}{\lambda}\theta_o(g,h)\Big) \\ exp\Big[-j\frac{2\pi}{\lambda z_2}[(m\Delta_r - Mk_1\Delta_s)g\Delta_a + (n\Delta_r - Ml_1\Delta_s)h\Delta_a]\Big] \tag{12}$$

Rewriting this equation so that the Δ's are implied, setting $a = Mk_1$ and $b = Ml_1$, doing a change of coordinates to to an ideal image (which removes the effect of magnification and inversion from the equations) [8, p. 131], assuming the system is otherwise shift invariant, and defining an output star location at α, β, which is at pixel coordinates a, b, the final form is found to be:

$$h_a(m-a, n-b) = \frac{\Delta_a^2}{\lambda^2 z_1 z_2 |M|} \sum_{g=1}^{N} \sum_{h=1}^{N} \Big[P(g,h) exp\Big(j\frac{2\pi}{\lambda}\theta_o(g,h)\Big) exp\Big[-j\frac{2\pi}{\lambda z_2}[(m-a)g + (n-b)h]\Big]\Big] \tag{13}$$

where as a reminder the M is the system transverse magnification.

A model is now available to represent the optical transfer function for a linear system that generated light by a single star and propagated it through the optical system of the star tracker, and imaged on the FPD with optical aberrations.

Equation (14) below gives the required pixel pitch of the detector,

$$\Delta_{det} < \frac{\lambda f_l}{2D} \tag{14}$$

The factor that is used in this discussion will be called *blur*, and is equal to the ratio of the pixel size to the Nyquist size. It is calculated as follows

$$blur = \frac{d}{\frac{\lambda f_l}{2D}} \tag{15}$$

where d is again the pixel pitch of the sensor, and the denominator is the Nyquist sampling of Equation (14).

The calculated power at the detector with under-sampling is computed using the convolution of the input power waveform with the undersampled PSF waveform, as discussed and shown in Equation (9), to get the power waveform with the diffraction effects as follows:

$$I_{det}(m_1\Delta_x, n_1\Delta_y) = \Delta_s^2 \sum_{m=1}^{N} \sum_{n=1}^{N} I_{in}(m\Delta_x, n\Delta_y) h(Pm_1\Delta_x - m\Delta s, Pn_1\Delta_y - n\Delta_s) \tag{16}$$

where in this case P = $blur$ and is the image under-sampling factor and represents how many samples are being skipped.

If the Nyquist sampling is not met by the detector (undersampled, or not satisfying Equation (14)), one has to include a new factor in the PSF, which is the effect of the detector integration. The overall PSF will change; the change is the PSF of the optics, h convolved with a rectangle that is the size of the detector pixel. Therefore if under-sampled, the detector is blurring and adding to the convolution.

If one is sampling with the pixel size $blur = P$ times the size of the Nyquist size as given in Equation (14), the undersampled PSF is found by looking at the PSF for the system without sampling, and then convolving it with a rectangle function the size of P. Therefore, if h is the optical PSF without sampling, the total PSF, h_{us}, is found by the following

$$h_{us}(m_1\Delta_x, n_1\Delta_y) = \Delta_x\Delta_y \sum_{p=1}^{N}\sum_{q=1}^{N} h(p\Delta_x, q\Delta_y)\text{rect}\left(\frac{(m_1-p)\Delta_x}{P}\right)\text{rect}\left(\frac{(n_1-q)\Delta_y}{P}\right) \tag{17}$$

where m_1 and n_1 are the coordinates of the new PSF and p and q are the coordinates of the points of the input PSF.

3. DETECTION AND ESTIMATION

Detection algorithms are needed to analyze the star tracker image and determine whether a star is present or not in a particular pixel. This determination is affected by the noise present on the detector.

The receiver operating curve (ROC) is a plot used to compare the performance of a detector or detection scheme versus another [10]. It will be used to evaluate which detection scheme is the best in this analysis. The probability of detection and false alarm in general can be found by the following equations [10]

$$P_d = \int_{-\infty}^{T_\Lambda} P(\Lambda|H_1)\delta\Lambda \tag{18}$$

and

$$P_{fa} = \int_{-\infty}^{T_\Lambda} P(\Lambda|H_0)\delta\Lambda \tag{19}$$

which show each as an integration of the probabiliy density function (PDF) of the likelihood ratio test (LRT), Λ. The range of integration goes to T_Λ, which is the threshold value for the LRT. To create the ROC, these will be plotted against each other.

3.1 Binary Hypothesis Testing (BHT)

The Binary Hypothesis Testing (BHT) is a simple threshold operation for a given point on the image plane. It is the formulation of a test, the LRT, of which the output is compared to a threshold value. This LRT, denoted as Λ, is defined to be [11, p. 65]

$$\Lambda = \frac{P(d(x,y)|H_1)}{P(d(x,y)|H_0)} > \gamma \tag{20}$$

where γ is the threshold, $d(x,y)$ is the image data at pixel coordinates (x,y), H_0 and H_1 are the binary hypothesis referred to as the null hypothesis and the alternative hypothesis, respectively. The $P(d(x,y)|H_i)$ is the joint conditional probability of the data given hypothesis H_i where i is either 0 or 1.

The value of γ is found by choosing a probability of false alarm, P_{fa}, which is discussed further in the next chapter, and finding the γ in the following equation

$$P_{fa}(\gamma) = \int_{\gamma}^{\infty} P(x|H_0)dx \tag{21}$$

Where the range of integration is denoted by the values that make the LRT greater than γ. See Appendix 3A in [11] for the development of Equation (21).

3.2 Matched Filter

The idea of a matched filter is to correlate the expected received signal with the actual received signal. This is represented by the following equation:

$$C = \sum_{y}\sum_{x} d(x,y)h_{opt}(x,y) \tag{22}$$

where C is the resulting correlation output, the y and x values are the pixel ranges in each dimension, the $d(x,y)$ is the received intensity at location (x,y), and the $h_{opt}(x,y)$ is the intensity PSF determined for the optical system.

The value C is then compared to a threshold to determine if there is a signal present or not.

3.3 Multi Hypothesis Testing (MHT)

The MHT uses an intensity PSF model to do correlations of multiple-shifted PSF models with the star signal. The research plans to leverage previous work done in the area of Multi-hypothesis testing [12]. This approach is used to improve on the probability of detection in the case the image of a space object that does not fall in the center of the pixel. The approach is used on an undersampled imaging system, to take advantage of the aliasing effects of the PSF [12, p. 2]. The test is to select one hypothesis, H_k over all other hypotheses by finding the one that has the highest overall probability.

$$k_{max} = \max_{k} P(x|H_k) \tag{23}$$

Where k_{max} is the hypothesis with the highest conditional probability, and k spans over the number of hypothesis. Deriving a Signal to Noise Ratio (SNR) assuming the noise on the image is Gaussian, the cited paper above from Zingarelli, et al., shows that the maximum likelihood (ML) decision rule used for a pixel divided into nine regions, giving 10 possible hypothesis is:

$$SNR_a = \frac{\sum_{w}^{M_d}\sum_{z}^{M_d}(d(w,z)-B)h_{samp}(w+c_x-\alpha_a, z+c_y-\beta_a)}{\zeta\sqrt{\sum_{w}^{M_d}\sum_{z}^{M_d}h_{samp}^2(w,z)}} \underset{H_o}{\overset{H_a}{\gtrless}} \gamma_{M-ary} \tag{24}$$

where $d(w,z)$ is the background suppressed image data, h_{samp} is the undersampled intensity PSF found previously, c_x and c_y are the coordinates of the pixel being tested, and the values of α_a and β_a are the horizontal and vertical sub-pixel shifts of the PSF, to dither it to one of nine locations in a pixel, and B is the background light.

The H_o is the hypothesis that no object is present, and H_1 to H_9 or the hypothesis that an object is present in the dithered mapped sub-pixel locations. It is shown in [12] that the MHT technique can provide an increase in detection performance, and can be used to provide sub-pixel position information and more accurate estimates of object irradiance.

The technique used in these results will be evaluated for use in determining star positions with star trackers. There is an opportunity to evaluate a trade-off in using a certain number of hypotheses M, with the computation required, along with the additional positional information that can obtained from centroiding.

Once the thresholding has been done, one can decide if there is starlight in each pixel, and in the case of the MHT, where in that pixel to M divisions (9 was used in [12]). The problem now turns to using this data to calculate the most accurate location estimation possible.

3.4 Centroiding

The stars are considered a spatial impulse response, and in many cases a star, when focused correctly onto the FPD, will fit inside of a pixel. In order for centroiding to result in a star location with sub-pixel accuracy, the optics are designed to generate a slightly out-of-focus star that occupies several pixels. It is shown that the centroiding accuracy

is a function of the size of the PSF, the photoelectrons the star generates, and the noise level added to the star signal [13, p. 592]. However, the centroiding does not improve the accuracy until the PSF radius gets larger than 0.5 pixels, since the entire PSF could be contained in one pixel. Therefore, given that the star light encompasses several pixels, the following describes the centroiding technique.

Using the threshold detection results discussed previously, star clusters are generated, which means that the pixels that are grouped together are algorithmically assigned to a particular star [14]. When that is complete, a region of interest (ROI) is defined which is a window of pixels surrounding the cluster. The next step is to subtract off the noise floor from all of the pixels in the ROI, giving just pixels with values of star photon signal only. The centroid, or sometimes called the weighted sum technique, of the star is then calculated by the following equations [13]

$$B_{ROI} = \sum_{x=R_s+1}^{R_e-1} \sum_{y=R_s+1}^{R_e-1} \Big(d(x,y) - N_b \Big) \tag{25}$$

$$c_x = \sum_{x=R_s+1}^{R_e-1} \sum_{y=R_s+1}^{R_e-1} \frac{x \cdot d(x,y)}{B_{ROI}} \tag{26}$$

$$c_y = \sum_{x=R_s+1}^{R_e-1} \sum_{y=R_s+1}^{R_e-1} \frac{y \cdot d(x,y)}{B_{ROI}} \tag{27}$$

Where the B_{ROI} is the total number of photons in the entire ROI, R_s and R_e are the ROI start and end respectively, the c_x and c_y are the centroid values of the x and y locations on the array, the $d(x,y)$ is the number of photons at the pixel located at the coordinates x and y, and N_b is the background intensity without a star present.

3.5 Using MHT along with Centroiding

One could use the MHT technique along with the centroiding approach to potentially gain more sub-pixel accuracy. If one includes not only the pixel data values in the ROI, but further divide those into the sub-pixel regions defined in the MHT algorithm, the total accuracy may be increased. This is accomplished by using the SNR found in Equation (24), where each hypothesis returns a SNR value. When one uses these SNR values with the centroiding technique along with their subpixel locations as defined in the MHT approach, it is found in [15, p. 65] that this method provides a total error of over 3 times less than the traditional centroid method. The total number of subpixel values used in the MHT method will need to be optimized and this could be the topic of future research.

4. ACCURACY BOUND ON THE ESTIMATION

To understand how well one can determine where that star is located, a bound on the position estimate for a given star at α, β is desired. Specifically, a lower bound on the estimate is of interest, and the model can be reduced to one star with just one type of noise on the signal. Since other stars produce noise, and if the signal has other types of noise on it, that will only increase the error in the actual measurement, and won't effect the goal of obtaining a lower bound solution.

The ability to estimate the star image on the focal plane has limits to its accuracy. For an unbiased estimate it can be shown that the lower bound on the variance of an estimator of one parameter is given by the Cramer Rao bound as follows [16]:

$$\text{var}(\hat{\alpha}) \geq \left[-E\left[\frac{\partial^2 (lnP(D;\alpha))}{\partial \alpha^2} \right] \right]^{-1} \tag{28}$$

Where var is the variance operation, E is the expectation operator, $P(D;\alpha)$ is the probability of the data received by the sensor, D, with a parameter value of α.

For the star location estimation problem, there are two parameters that need to be estimated, (α, β), the coordinates of the location on the focal plane; in this case one can find the Information Matrix

$$\mathbf{I}(\Theta) = \begin{bmatrix} -E\left[\frac{\partial^2(lnP(D;\Theta))}{\partial\alpha^2}\right] & -E\left[\frac{\partial^2(lnP(D;\Theta))}{\partial\alpha\partial\beta}\right] \\ -E\left[\frac{\partial^2(lnP(D;\Theta))}{\partial\alpha\partial\beta}\right] & -E\left[\frac{\partial^2(lnP(D;\Theta))}{\partial\beta^2}\right] \end{bmatrix} \tag{29}$$

where Θ is the vector $\begin{bmatrix}\alpha & \beta\end{bmatrix}^T$.

The CRLB is then found for each parameter being estimated as

$$\text{var}(\Theta) \geq [\mathbf{I}^{-1}(\Theta)]_{ii} \tag{30}$$

where i has values of 1 and 2, and ii are the $[11]$ and $[22]$ elements in the inverse $2x2$ matrix, $\mathbf{I}^{-1}$.

4.1 Likelihood Function

Understanding and defining the probability of the data given that the star is projected on a particular pixel location, $P(D;\Theta)$, for the optical system under consideration is the first step in developing an analytical solution to the accuracy bound in Equation (30). The data, $d(u,v)$, received from a star can be considered to have a Poisson distribution, representing the number of photons at the pixel during a given interval of time. The data received can be written as

$$d(u,v) = i(u,v) + n(u,v) \tag{31}$$

where $i(u,v)$ is the image equation, and is the mean of the data, and therefore not a random variable, and n is zero mean additive noise; however, one should note that $n(u,v)$ does not have a Gaussian distribution.

$d(u,v)$, when sampled by a FPD, is the photon measurement at each of the sensor pixels m,n and is therefore an integer and has a single value over the entire pixel. The image created by one star and written in terms of pixels is as follows

$$i(m,n) = \gamma_1 h(m\Delta_r - a\Delta_r, n\Delta_r - b\Delta_r) + B \tag{32}$$

where $\alpha = a\Delta_r$, $\beta = b\Delta_r$. This will be written with the $\Delta' s$ implicit as follows

$$i(m,n) = \gamma_1 h(m-a, n-b) + B \tag{33}$$

Using the equation for a Poisson probability mass function (PMF), the distribution of one pixel of the data, m_1, n_1, is the following

$$P(D = d(m_1,n_1;a,b)) = \frac{i(m_1,n_1)^{d(m_1,n_1)} e^{-i(m_1,n_1)}}{d(m_1,n_1)!} \tag{34}$$

where D is a random variable representing the data received, $d(m_1,n_1)$ is the data received at the pixel m_1,n_1, and (a,b) is inserted for the vector Θ as the parameters representing the center of the image $i(m,n)$.

If one considers all of the pixel locations m,n within the array encompassing the total image, the probability is given by

$$P(D;a,b) = \prod_m \prod_n \frac{i(m,n)^{d(m,n)} e^{-i(m,n)}}{d(m,n)!} \tag{35}$$

where the first product sign is over all the pixel array in the u direction, and the second is over all the pixel array in the v direction. This operation assumes that the probabilities of each pixel location are independent of each other. It is from this equation, which is called the Likelihood Function, that we proceed to evaluate the Cramer Rao limit given in Equation (30) and Equation(29) above. If the partial of the distribution function with respect to one of the parameters

doesn't result in a function of the other, then the reciprocal of the diagonal elements of the Information Matrix will be the lower bound of the variance of the parameters m,n respectively. In other words, if the probabilities of the x and y directions are independent of each other, in which one direction does not effect the other, the reciprocal of the diagonal elements can be used. Therefore if this is the case, Equation (30) can be written as

$$var(\hat{a}) \geq \frac{1}{\mathbf{I}_{11}} \tag{36}$$

and

$$var(\hat{b}) \geq \frac{1}{\mathbf{I}_{22}} \tag{37}$$

where the indices equations can be found in the $\mathbf{I}$ of Equation (29).

The first step, therefore, will be to find the bound for parameter a using Equation (29) and Equation (36).

Taking the natural log of each of the sides in Equation (35), the Log Likelihood, $\mathbf{L}$, is obtained

$$\mathbf{L} = \ln P(D;a,b) = \sum_m \sum_n [d(m,n) \ln i(m,n) - i(m,n) - \ln(d(m,n)!)] \tag{38}$$

where the terms are now summed due to the property of the log function.

4.2 Finding the Cramer Rao Lower Bound

The steps to find the Cramer Rao bound are as follows:

1. Taking the partial with respect to parameter a, of Equation (38).
2. Taking the partial again of that result with respect to a.
3. Following Equation (29) of the first row and first column of the Fishers Information 2 X 2 matrix, one needs to find the expectation of that previous result.
4. The negative of the result of the last step can be used to find the first row and first column of the Fishers Information 2 X 2 matrix of Equation (29) [16], and then to find the bound from Equation (36).

The result of these steps is found to be:

$$var(\hat{a}) \geq \left[\sum_m \sum_n \frac{1}{i(m,n)} \left[\frac{\partial i(m,n)}{\partial a} \right]^2 \right]^{-1} \tag{39}$$

where again the summation is done over the range of m and n, which are the pixel indices of the FPD.

4.3 Finding the PSF

A star can be modeled in an optical system as a spatial impulse function. The image on the detector of the star tracker can be represented by Equation (33) where $i(m,n)$ is the image created on the detector array, γ_1 is the brightness of the star, and $h(m-a,n-b)$ is the PSF centered at the coordinate indices of a,b, and B is the background noise.

Equation (13) can be used to find the $h(m-a,n-b)$, which is the PSF for an incoherent star source, which can be put directly into the image equation.

Note this equation is described in terms of the indices of the samples for each of the planes of interest – the source, aperture, and the receive (or image) planes as described in Figure 3. The star image, which is an incoherent source, is linear in intensity, so the impulse response of such a system is the squared magnitude of the amplitude impulse response [8, p. 133]. This squared term is used in Equation (11) to calculate the OTF. Since the amplitude PSF is given by Equation (13), one can find its squared magnitude to give the desired impulse response of the system under consideration.

This is evaluated below.

$$h(m-a,n-b) = PSF = |h_a(m-a,n-b)|^2 = \left(\frac{\Delta_a^2}{\lambda^2 z_1 z_2 |M|}\right)^2 \left[\sum_{g=1}^{N}\sum_{h=1}^{N}\left[P(g,h)exp\Big(j\frac{2\pi}{\lambda}\theta_o(g,h)\Big)exp\Big[-j\frac{2\pi}{\lambda z_2}[(m-a)g+(n-b)h]\Big]\right]\right] \left[\sum_{g=1}^{N}\sum_{h=1}^{N}\left[P(g,h)exp\Big(-j\frac{2\pi}{\lambda}\theta_o(g,h)\Big)exp\Big[+j\frac{2\pi}{\lambda z_2}[(m-a)g+(n-b)h]\Big]\right]\right] \quad (40)$$

where $\theta_o(g,h)$ is the aberration distortion phase.

4.4 Under-sampling Effect on the PSF

Equation (40) gives the intensity of the PSF when sampled at Nyquist, and without any under-sampling considerations. The following will take into account the pixel size on the FPD and how that effects the received PSF. This is represented by a convolution of a two dimensional rectangle function the size of a pixel with the PSF calculated in Equation (40), as found in Equation (17). Simplifying by setting

$$k_2 = \left(\frac{\Delta_a^2}{\lambda^2 z_1 z_2 |M|}\right)^2 \quad (41)$$

the convolution becomes

$$PSF_s = h_s(m-a,n-b) = k_2 \sum_{m_N}\sum_{n_N}\left\{rect\Big(\frac{(m-m_N)}{P}\Big)rect\Big(\frac{(n-n_N)}{P}\Big) \left[\sum_{g=1}^{N}\sum_{h=1}^{N}\left[P(g,h)exp\Big(j\frac{2\pi}{\lambda}\theta_o(g,h)\Big)exp\Big[-j\frac{2\pi}{\lambda z_2}[(m_N-a)g+(n_N-b)h]\Big]\right]\right] \left[\sum_{g=1}^{N}\sum_{h=1}^{N}\left[P(g,h)exp\Big(-j\frac{2\pi}{\lambda}\theta_o(g,h)\Big)exp\Big[+j\frac{2\pi}{\lambda z_2}[(m_N-a)g+(n_N-b)h]\Big]\right]\right]\right\} \quad (42)$$

where the image indices m_N, n_N, are the Nyquist samples in the convolution for the two dimensional rectangle function and replace the PSF expression sampling, and the P is the undersampling factor of the m_N, n_N indices.

4.5 Completing the Undersampled Defocused CRLB Analytical Equation

One can make a substitution using the following assignments:

$$S_1(m_N,n_N,a,b) = \sum_{g=1}^{N}\sum_{h=1}^{N}P(g,h)exp\Big(j\frac{2\pi}{\lambda}\theta_o(g,h)\Big)exp\Big[-j\frac{2\pi}{\lambda z_2}[(m_N-a)g+(n_N-b)h]\Big] \quad (43)$$

$$S_2(m_N,n_N,a,b) = \sum_{g=1}^{N}\sum_{h=1}^{N}P(g,h)exp\Big(-j\frac{2\pi}{\lambda}\theta_o(g,h)\Big)exp\Big[+j\frac{2\pi}{\lambda z_2}[(m_N-a)g+(n_N-b)h]\Big] \quad (44)$$

Using Equation (33), and inserting Equations (42), (43), and (44), and then applying Equation (39), and using the additional substitutions:

$$S_3(m_N,n_N,a,b) = \sum_{g=1}^{N}\sum_{h=1}^{N}\left[P(g,h)exp\Big(-j\frac{2\pi}{\lambda}\theta_o(g,h)\Big)exp\Big[+j\frac{2\pi}{\lambda z_2}[(m_N-a)g+(n_N-b)h]\Big]\Big(-j\frac{2\pi}{\lambda z_2}x\Big)\right] \quad (45)$$

$$S_4(m_N,n_N,a,b)=\sum_{g=1}^{N}\sum_{h=1}^{N}\left[P(g,h)exp\Big(j\frac{2\pi}{\lambda}\theta_o(g,h)\Big)exp\Big[-j\frac{2\pi}{\lambda z_2}[(m_N-a)g+(n_N-b)h]\Big]\Big(j\frac{2\pi}{\lambda z_2}x\Big)\right] \tag{46}$$

$$R_1=rect\Big(\frac{(m-m_N)}{P}\Big)rect\Big(\frac{(n-n_N)}{P}\Big) \tag{47}$$

results in, setting $k_3=\gamma_1 k_2$,

$$var(\hat{a})\geq\left\{\sum_m\sum_n\left\{\left[\frac{1}{k_3\left\{\sum_{m_N}\sum_{n_N}\left(rect\Big(\frac{(m-m_N)}{P}\Big)rect\Big(\frac{(n-n_N)}{P}\Big)S_1S_2\right)+B\right\}}\right]\right.\right.$$
$$\left.\left.\left[k_3\sum_{m_N}\sum_{n_N}\left\{rect\Big(\frac{(m-m_N)}{P}\Big)rect\Big(\frac{(n-n_N)}{P}\Big)\Big[S_1S_3+S_2S_4\Big]\right\}\right]^2\right\}\right\}^{-1} \tag{48}$$

Note the S_i expressions are summations over the pupil indices g,h of variables x,y which are a function of the indices m,n of variables u,v and shifted by indices a,b of location variables α,β (the variables being estimated).

With the relationship of Equation (48) to determine the Cramer Rao bound for the star image location estimate on the FPD, one can use it to evaluate it on the computer.

5. SIMULATION RESULTS

5.1 Cramer Rao Bound Analysis

The plot of the CRLB analytical solution of Equation (48) with respect to changing defocus with the system $blur=40$ is shown in Figure 5. The star tracker used has a focal length of $90mm$ and is defocused by increments of $10\mu m$ for a total of $1000\mu m$. The simulation runs from an in-focus point of $z_2=90mm$ to the out-of-focus point at $z_2=91mm$ (see Figure 4 to remind oneself of the notation). The y axis gives plots for the statistical lower bound on the variance for an estimator of the star image location on the focal plane on the left, and the log of that variance on the right. Note that this variance amplitude is normalized (an arbitrary value of the constant k_3 in Equation 48 was used) and is used to examine the relative and minimum values.

One can see that a minimum variance bound is achieved at a defocus of 50 μ m for this particular system. The parameters used for the simulation in this chapter are summarized for convenience in Table 1.

Table 1: Summary of Parameters Used for Model Simulation

PARAMETER	VALUE
aperture	0.05m
f-number	1.8
focal length	0.09m
CCD pixels	1024X1024
pixel size	18 μm
CCD sensor size	18.4 mm square
wavelength	0.5 μm
FOV	11.67 deg
Right Ascension	06 hrs 45 min 20 seconds
Declination	-16 degrees 42 mins 47 seconds
PPM Star Catalog	various

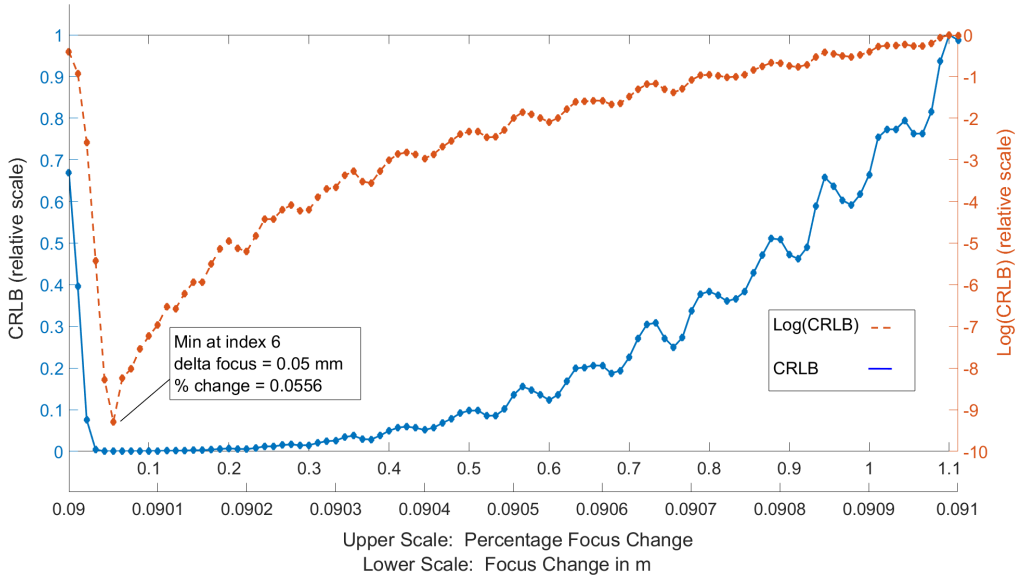


Fig. 5: Linear and Log Plots for the CLRB Analytical Solution versus Defocus for the Star Tracker with $blur = 40$ value.

5.2 Monte Carlo Analysis

A Monte Carlo program was used to generate a mean squared error of the estimator for the location of the star image on the CCD as follows

$$MSE(\hat{x}) = E_{\hat{x}}[(\hat{x} - x_t)^2] \tag{49}$$

where $\hat{x}$ is the x coordinate estimate of the star image on the focal plane, $E_{\hat{x}}$ is the expectation operator, and x_t is the actual value, or the truth value, in the simulation. This truth value is calculated by the geometry of the optics and the star location on the celestial sphere found with the help of the star catalog. Equation (49) can be put in terms of $\hat{y}$ for the y coordinate estimate, and the attitude estimate parameters of Right Ascension, $\hat{RA}$, Declination, $\hat{Dec}$, and Roll, $\hat{Roll}$ to find the MSE of those, respectively.

5.3 Monte Carlo Simulation Results

A simulation run for an example star with the range of defocus from 0 to 0.5 mm in increments of 10 μm is shown in Figure 6, using different detection techniques.

Figure 7 shows the log of the MSE of the star location estimate on the focal plane as compared to the CRLB analytical solution.

The Monte Carlo results and the minimum defocus value line up very closely to the CRLB bound in the plot, which is again at 50 μ m. In addition, one can see that the MHT method is achieving a lower MSE than the Correlation, and that in turn a lower MSE than the Point algorithm.

To evaluate the MSE with respect to different magnitude stars, and therefore different SNR values, the plot of Figure 7 was repeated for different stars with different magnitudes on the same plot. This can be seen in Figure 8.

The plot of Figures 8 shows that the star with a larger SNR obtains a lower minimum. This is consistent with previous research results [13], [14], [17].

From the location of the stars on the focal plane, an attitude solution is found for each Monte Carlo Run. The attitude estimates include $\hat{RA}$, $\hat{Dec}$, and $\hat{Roll}$, and an MSE is calculated for the estimates of each of these. A plot showing these results with a Monte Carlo run for a defocus range of 0 to 0.5 mm in increments of 10 μm is shown in Figure 9, Figure 10, and Figure 11.

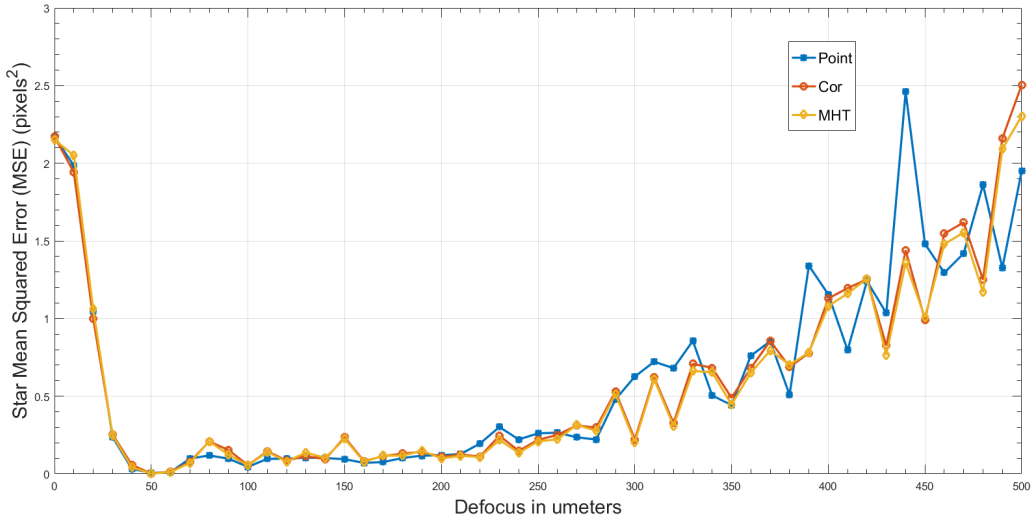


Fig. 6: Monte Carlo Run for calculating the MSE of an example star location position estimate versus defocus.

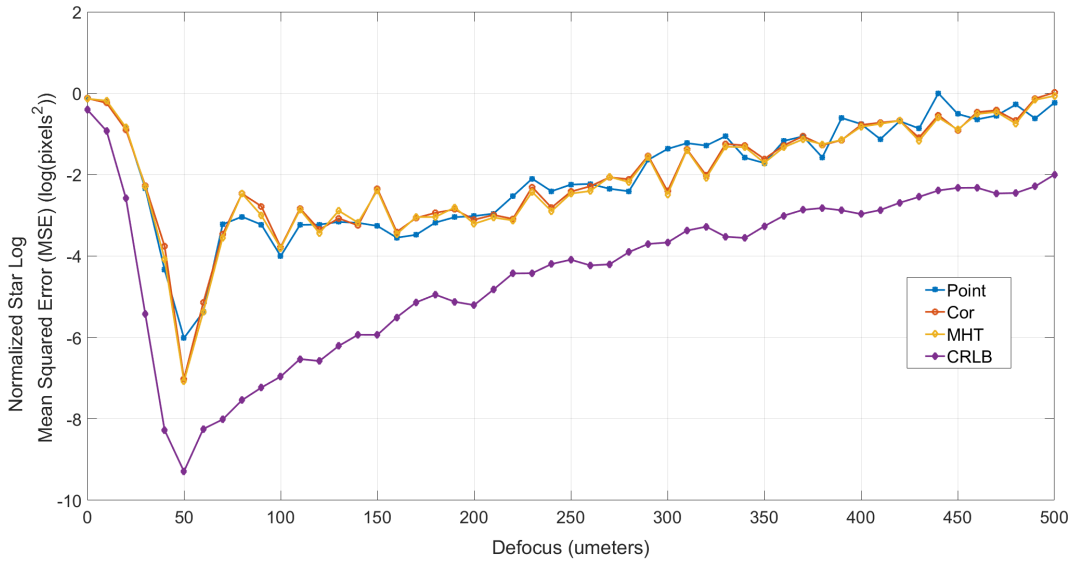


Fig. 7: The Star Position Mean Squared Error (MSE) Compared to the CRLB. The Plots are Scaled for Relative Comparison and on a Log Scale.

To compare the attitude solution parameters to the CRLB analytical solution, they are plotted together in Figure 12.

The plot of Figure 12 shows that the minimum for the attitude parameters line up very well with the minimum of the CRLB plot.

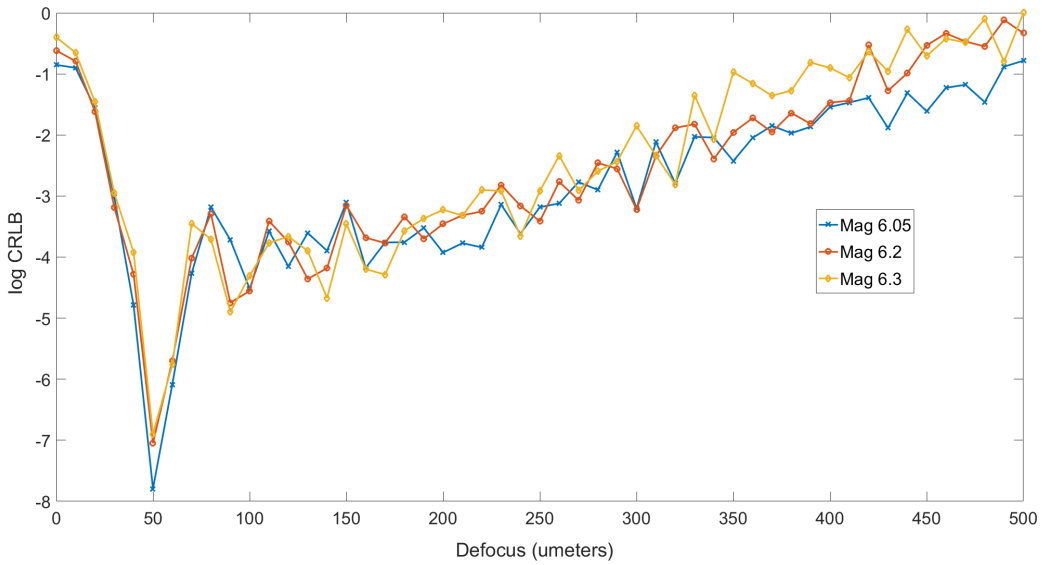


Fig. 8: A comparison of the MSE results for different magnitude stars.

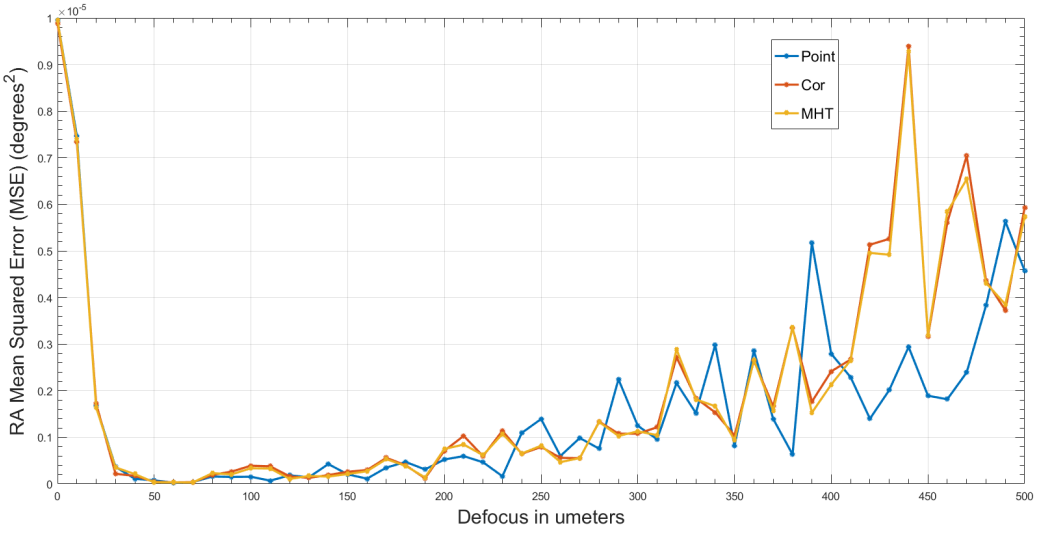


Fig. 9: Plot of the MSE for a Monte Carlo Run of the Right Ascension Estimates as a function of defocus.

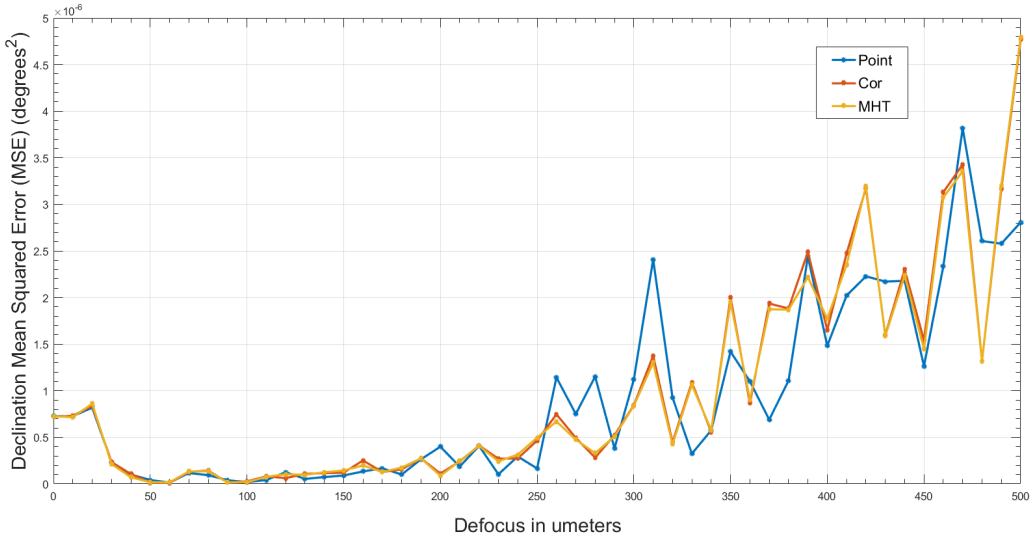


Fig. 10: Plot of the MSE for a Monte Carlo Run of the Declination Estimates as a function of defocus.

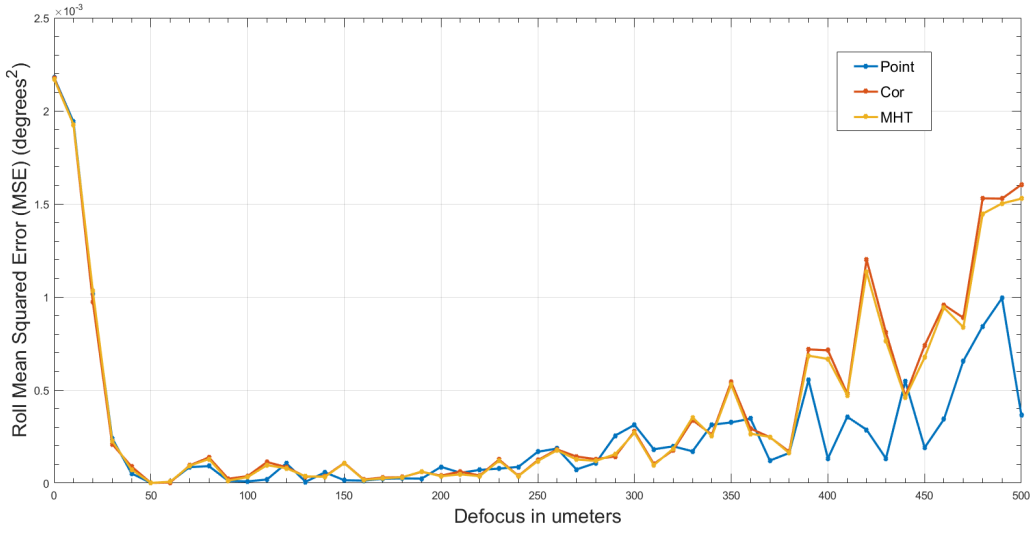


Fig. 11: Plot of the MSE for a Monte Carlo Run of the Roll Estimates as a function of defocus.

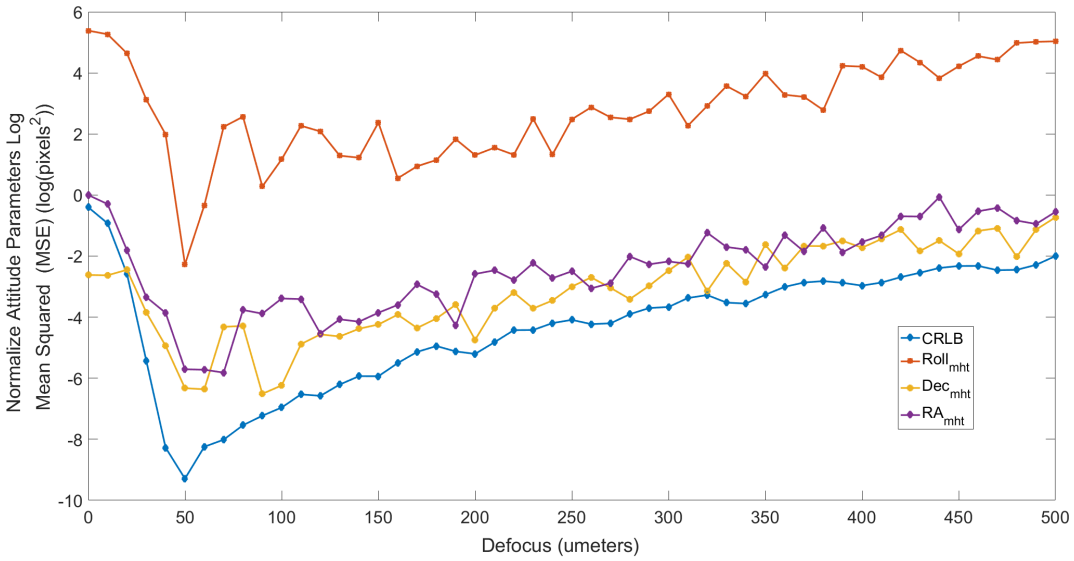


Fig. 12: The Attitude Parameters Mean Squared Error (MSE) Compared to the CRLB. The Plots are Scaled for Relative Comparison and on a Log Scale.

6. UNDERSAMPLING EFFECTS

The CRLB plot with no undersampling, or when $blur = 1$, is shown in Figure 13.

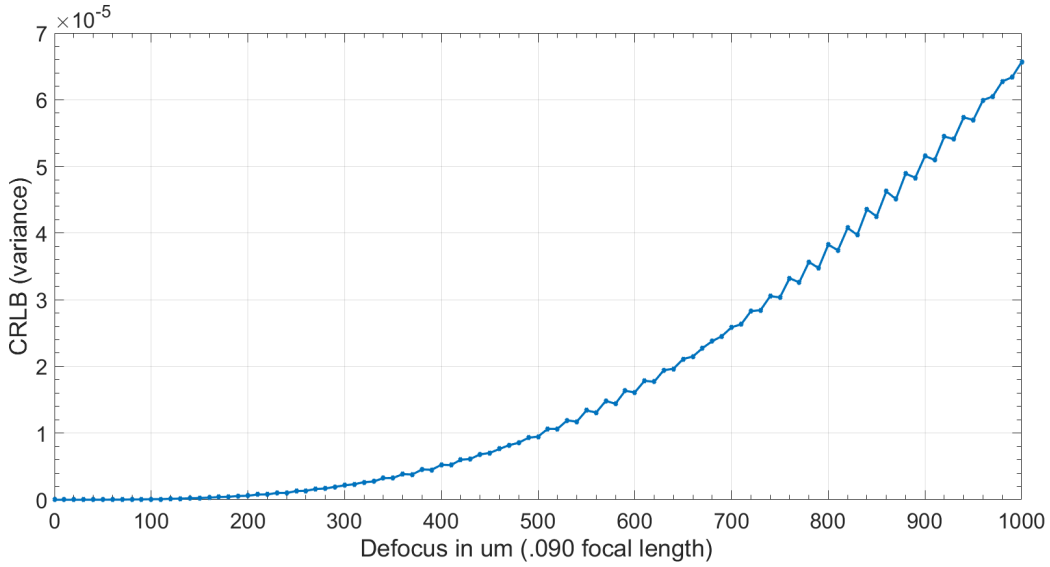


Fig. 13: Plot for the CLRB analytical solution versus defocus for thes tar tracker with no undersampling ($blur = 1$ value).

One can see that the variance for a properly sampled system at focus is very close to zero and increases with defocus. The following sections display the CRLB changes when the parameters of undersampling and defocus are changed.

6.1 CRLB as a function of defocus

The CRLB analytical solution of Equation 48 is shown in Figure 14 for a number of pixel pitch values versus a changing defocus. The plot is shown using the log of the CRLB value to better display the large range and the small values of variance.

6.2 CRLB as a function of pixel pitch

Conversely, the CRLB analytical solution of Equation 48 is shown in Figure 15, again a log plot, for a number of defocus values versus a changing pixel pitch.

6.3 CRLB as a function of both defocus and pixel pitch

The CRLB analytical solution of Equation 48 is plotted versus both defocus and pixel pitch in surface plots of Figure 16 and Figure 17, linear and log plots respectively.

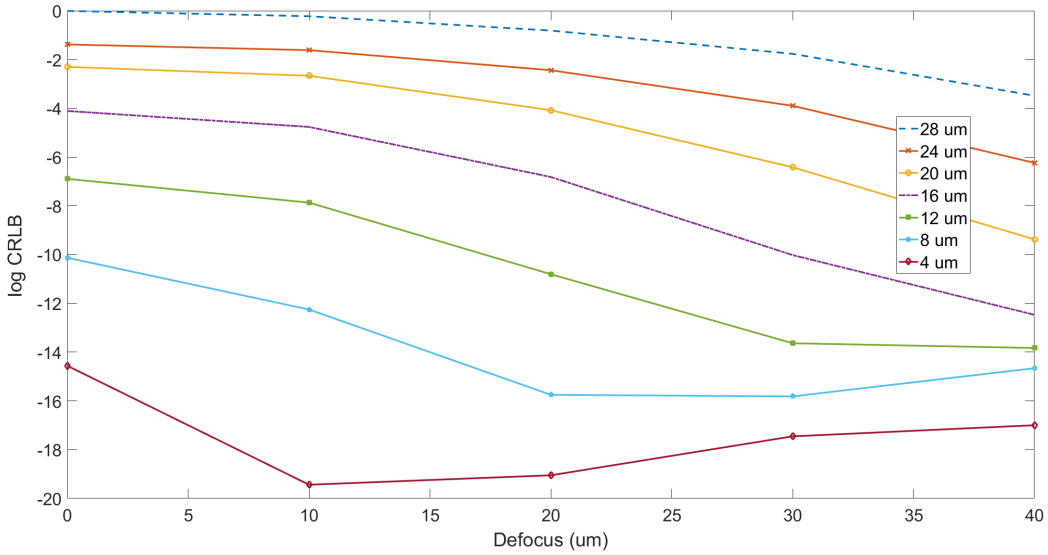


Fig. 14: Plot of the log CRLB versus defocus with different pixel pitch sampling on the focal plane.

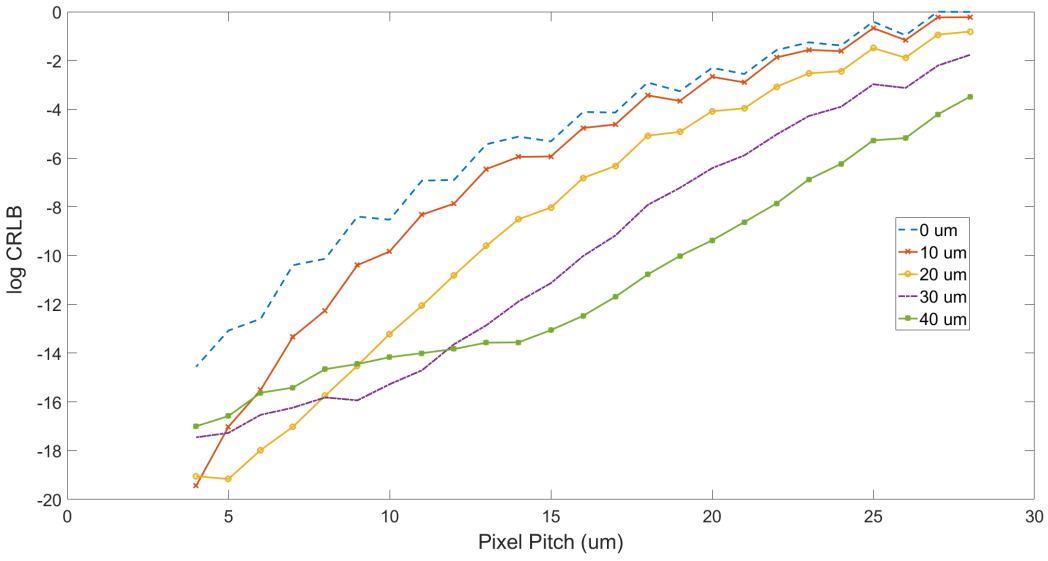


Fig. 15: Plot of the log CRLB versus pixel pitch size with different defocus values.

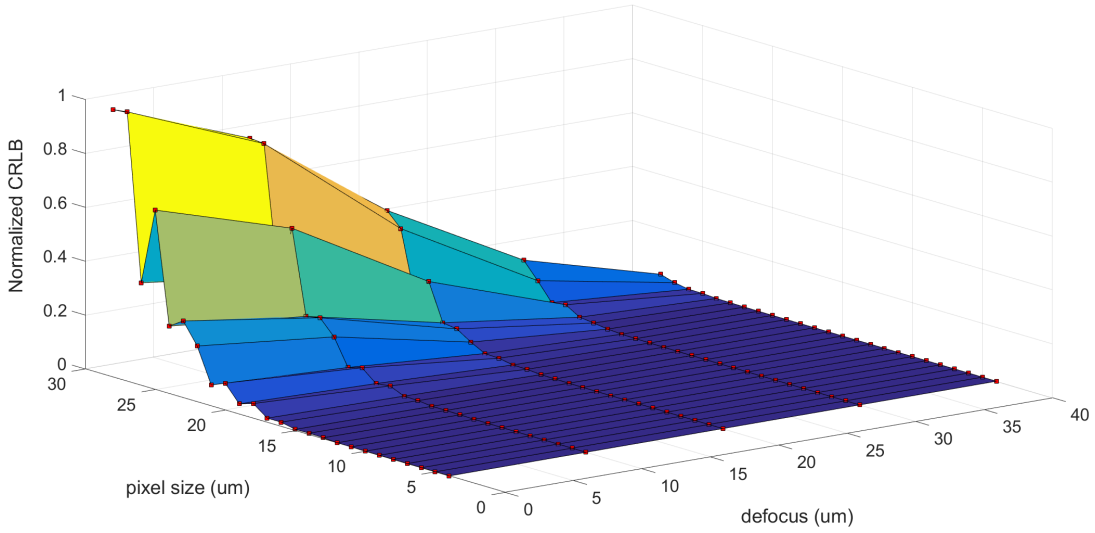


Fig. 16: Surface Plot of the CRLB versus both the defocus and the pixel pitch size.

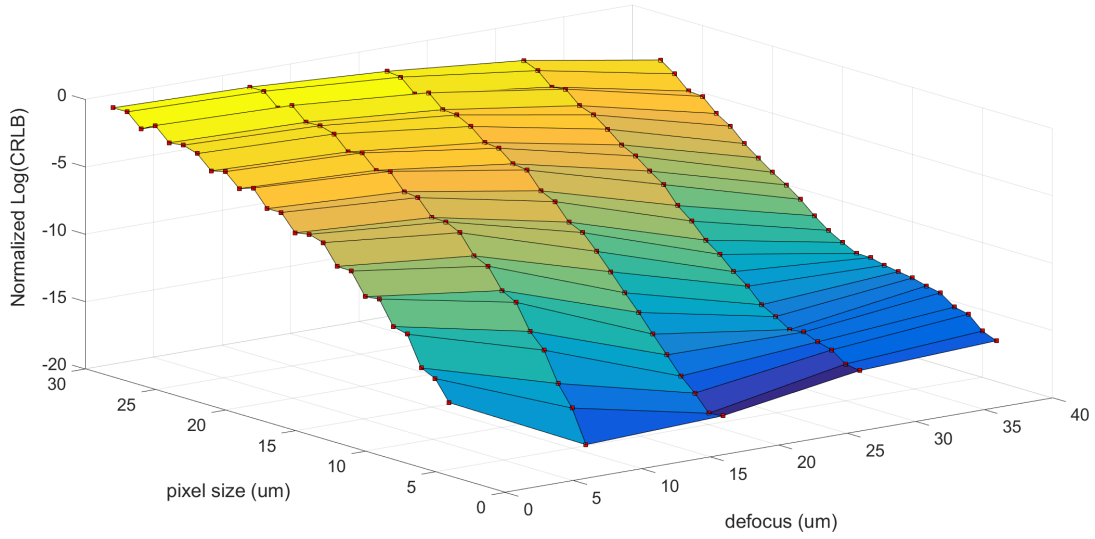


Fig. 17: Surface Plot of the Log CRLB versus both the defocus and the pixel pitch size.

7. SYSTEM ANALYSIS

7.1 Model Analysis

The previous results of the simulation show that the analytical CRLB result is validated by a working model of the star tracker system. This working model helped generate an independent statistical model through a Monte Carlo analysis. The results of the two were found to be similar and compatible with each other.

It is found that by looking at the surface plots of Figure 16 and Figure 17 one can see that in addition to an optimum defocus parameter, one must also consider what size sampling is being used on the FPD.

The plots of the calculated attitude using the star estimated locations found in Figure 12 show there is a good match between the lower bound variance location of the defocus with that of the star spot estimate on the FPD. This allows one to use the CRLB expression found in Equation 48 to minimize the variance of the estimate for the attitude parameters.

7.2 Comparing Optical Systems

The ability to compare two different star tracker system results – that is, systems with different undersampling and different f numbers, for example – is very important for understanding the general star tracker system design. Figure 18 shows a plot of the Monte Carlo variance of the star position versus the defocus for two different star tracker systems.

The following parameters were used for the two different systems in the analysis:

System 1: blur = 40, f/# = 1.8, focus = 0.09m, D = 0.05m, pixel pitch = 18 μm
System 2: blur = 16, f/# = 2, focus = 0.10m, D = 0.05m, pixel pitch = 8 μm

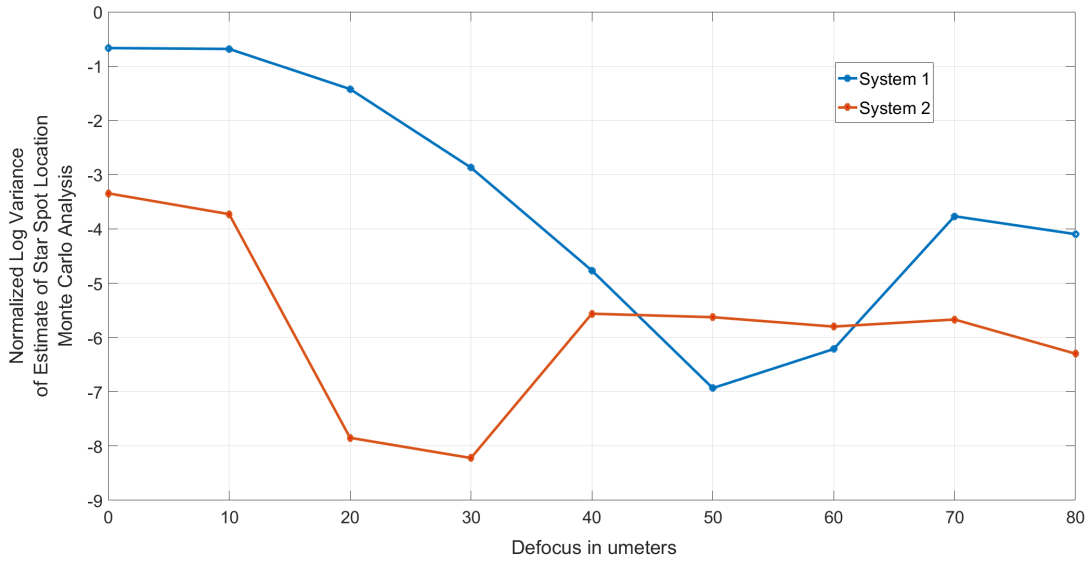


Fig. 18: Plot of the Monte Carlo variance of the star position versus the defocus for two different star tracker systems.

It is difficult to compare these two plots since the two optical and sensor parameters are different. To aid in this comparison, a relationship is derived for an estimate of the radius of the blur spot on the focal plane in units of pixels that is a function of the defocus, the pixel pitch value, and the f/# of the system. This derivation uses the geometry of the optical system as seen in Figure 19. The geometry assumes no aberrations.

The plot of each variance found is then plotted with respect to this new variable, which is the estimated pixel radius of the blur spot. This plot can be seen in Figure 20. It shows that each system variance of the estimated star position on the focal plane appear to have minimums at slightly different radius values. System 1 appears to have a minimum at the estimated radius of just above 0.77 pixels. System 2 appears to have a minimum at the estimate radius of just below 0.94 pixels.

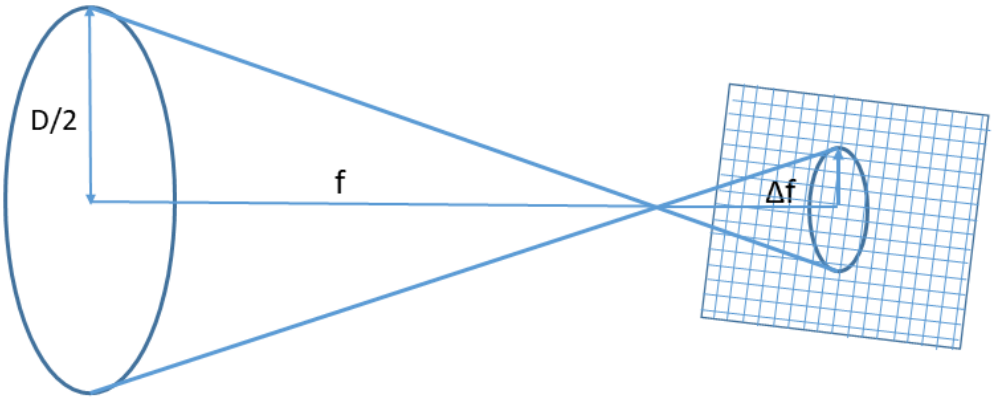


Fig. 19: The geometry of an optical system used to derive an estimate of the radius of the blur spot on the focal plane.

Further analysis is needed in this area; however the results above suggest that an optimum blur spot is dependent on what kind of undersampling is producing the acquired star image.

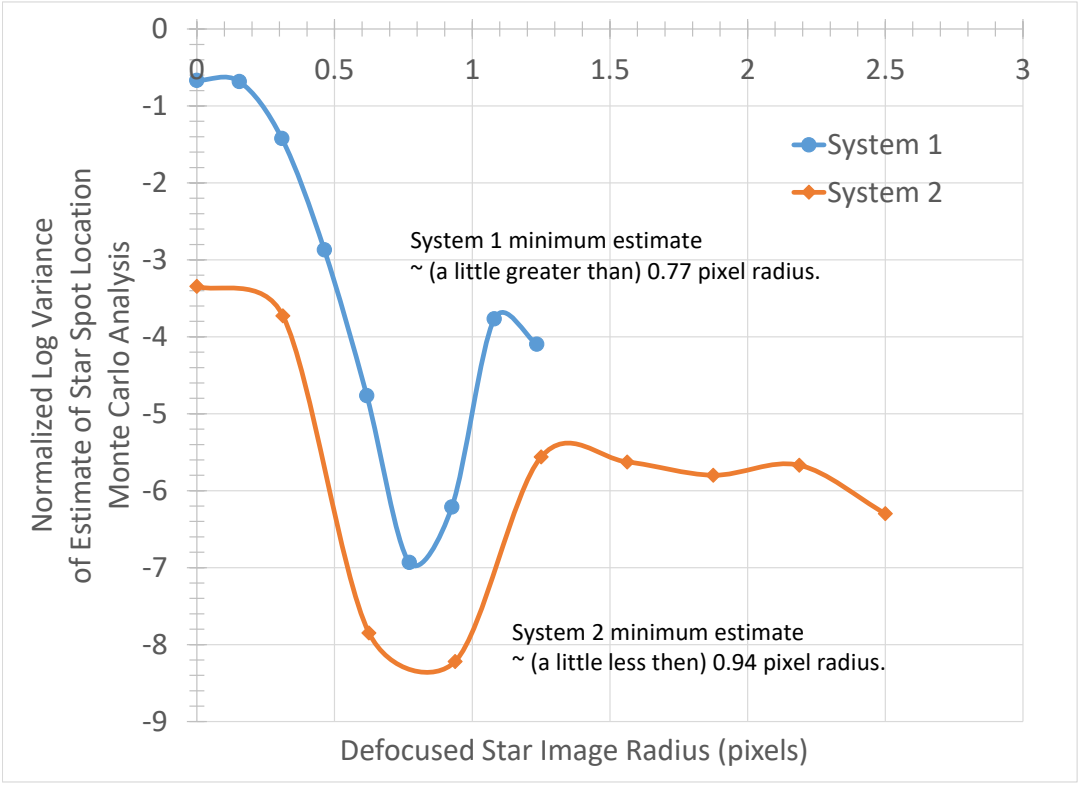


Fig. 20: Plot of the Monte Carlo Variance of the star position versus the star image radius in pixels for two different star tracker systems.

Another variable that is important for the accuracy of a system is the magnitude of the star. For completeness, the same plot for slightly different magnitude stars for a system is shown in Figure 21.

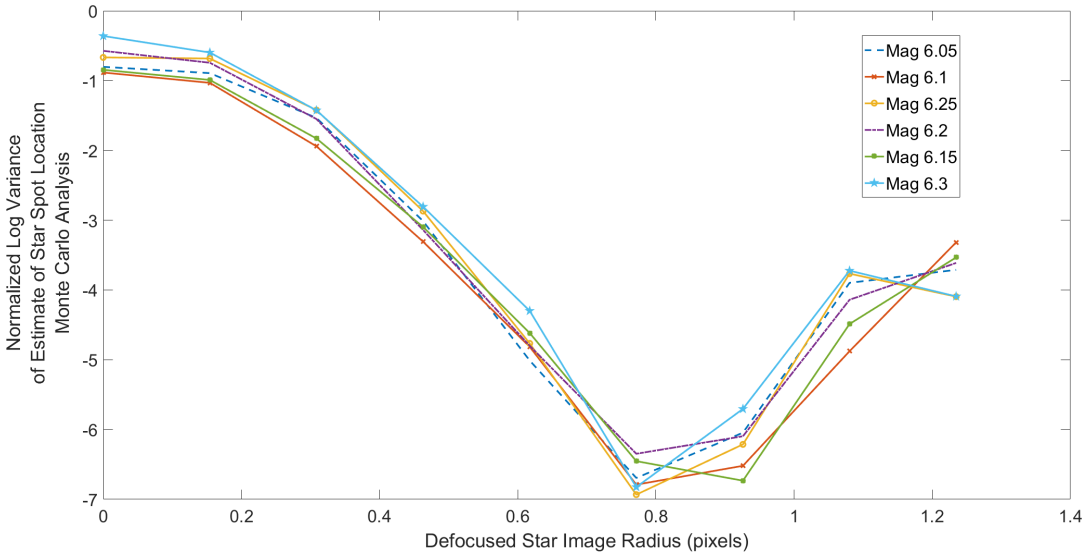


Fig. 21: Plot of the Monte Carlo variance of the star position versus the star image radius in pixels for a system with six different magnitude stars.

8. CONCLUSIONS AND FUTURE PLANS

The results validate the analytical CRLB result by a working statistical model of a star tracker system. The CRLB and the Monte Carlo analysis were each developed through independent methods and have solutions that correlate very well. Both the model and the CRLB analysis provide understanding of the parameters and their relationship to producing optimum accuracy of the star spot location estimates on the FPD array. It is also shown that the attitude minimum variance found with those star locations matches the corresponding CRLB minimum location of the star location estimates.

The results show that the analytical solution to the CRLB and the Monte Carlo simulations provide an ability for finding the optimum parameters for an optical system that produce the greatest accuracy in the attitude solution. The plot of Figure 20 gives insight into the focus and undersampling parameters that produce an optimum star image size giving the minimum variance or most accurate estimate. The model uses a PSF that is generated by using Fourier Optics and not using a Gaussian approximation, as has been done in the past. In addition, the undersampling effects are also applied by sampling that PSF per the actual pixel pitch. The model also takes into account the effects of different detection and estimation techniques on the estimate, so they can be evaluated. This work shows that the MHT detection and estimation technique appears to provide a more accurate solution to the estimate of the star positions on the FPD.

Forward work consist of the following areas:

- Further analysis of the relationship of the undersampling and defocus using the estimated blur spot size.
- Development of statistics involving the use of the MHT in a star tracker environment.
- Investigation of an optimum undersampling size using the MHT detection and estimation.
- Investigation of an optimum number of hypothesis using the MHT detection and estimation.

The results of this work hopefully have achieved the goal to provide insight into the parameters of an optical system and techniques for detection and estimation that give rise to the most accurate star tracker attitude output.

9. REFERENCES

[1] Donald M Cornwell. Nasa's optical communications program for 2015 and beyond. In *Free-Space Laser Communication and Atmospheric Propagation XXVII*, volume 9354, 2015.

[2] Donald M Cornwell. Nasa's optical communications program for 2017 and beyond. In *2017 IEEE International Conference on Space Optical Systems and Applications (ICSOS)*, pages 10–14. IEEE, 2017.

[3] Daniel E Raible, Robert R Romanofsky, James M Budinger, Jennifer Nappier, Alan Hylton, Aaron J Swank, and Anthony L Nerone. On the physical realizability of hybrid rf and optical communications platforms for deep space applications. In *32nd AIAA International Communications Satellite Systems Conference*, page 4482, 2014.

[4] Aaron J Swank, Eliot Aretskin-Hariton, Dzu K Le, Obed Sands, and Adam Wroblewski. Beaconless pointing for deep-space optical communication. In *34th AIAA International Communications Satellite Systems Conference*, page 5708, 2016.

[5] Daniel Raible, Robert Romanofsky, Gary Pease, and Thomas Kacpura. Integrated radio and optical communication (iroc). https://ntrs.nasa.gov/search.jsp?R=20160010290, 2016. NASA Technical Report Slide Presentation.

[6] Liheng Ma, Chunsheng Hu, Xingshu Wang, and Dongkai Dai. Advances and accuracy performance of the star trackers. In *ISPDI 2013-Fifth International Symposium on Photoelectronic Detection and Imaging*, pages 89080M–89080M. International Society for Optics and Photonics, 2013.

[7] Alexei V Filippenko. *Understanding the Universe: An Introduction to Astronomy*. Teaching Company, 2007.

[8] Joseph W Goodman. *Introduction to Fourier optics*. Roberts and Company Publishers, 2004.

[9] Tyler Hardy, Stephen Cain, Jae Jeon, and Travis Blake. Improving space domain awareness through unequal-cost multiple hypothesis testing in the space surveillance telescope. *Applied optics*, 54(17):5481–5494, 2015.

[10] Richard D. Richmond and Stephen C. Cain. *Direct Detection LADAR Systems*. 2010.

[11] Steven M Kay. *Fundamentals of Statistical Signal Processing. Detection Theory, Volume II*. Prentice Hall, Englewood Cliffs, New Jersey, 1998.

[12] J Chris Zingarelli, Eric Pearce, Richard Lambour, Travis Blake, Curtis JR Peterson, and Stephen Cain. Improving the space surveillance telescope's performance using multi-hypothesis testing. *The Astronomical Journal*, 147(5):111, 2014.

[13] Carl Christian Liebe. Accuracy performance of star trackers-a tutorial. *IEEE Transactions on aerospace and electronic systems*, 38(2):587–599, 2002.

[14] Kara Z Huffman. Designing star trackers to meet micro-satellite requirements. Technical report, 2006.

[15] Anthony J Sligar. Measuring angular rate of celestial objects using the space surveillance telescope. Technical report, Air Force Institute of Technlogy, Wright-Patterson AFB OH, Graduate School of Engineering and Management, 2015.

[16] Steven M Kay. *Fundamentals of statistical signal processing, volume I: estimation theory*. Prentice Hall, 1993.

[17] Kim A Winick. Cramer–rao lower bounds on the performance of charge-coupled-device optical position estimators. *JOSA A*, 3(11):1809–1815, 1986.